A Novel and Effective Surface Flaws Inspection Instrument for Large Aperture Optical Elements

Xian Tao, Zhengtao Zhang, *Member*, *IEEE*, Feng Zhang, De Xu, *Senior Member, IEEE*

Abstract—Surface defects on precision optical elements must be carefully inspected since they impact the normal operation of an optical system. It is a challenge to inspect defects of large aperture optical elements using an imaging system because of efficiency and accuracy. This paper designs a novel and effective inspection instrument with two imaging systems for large aperture optical elements. They are the dark-field imaging system (DFIS) with a line scan camera in 10μm resolution and the bright-field imaging system (BFIS) with a microscopic camera in 0.85μm resolution. To keep the clarity of DFIS in large scope quickly scanning, an adaptive scan path planning method is proposed. A set of novel algorithms is proposed to process a large number of dark-field images. Due to the limitations of DFIS in scattering effect, the corresponding bright-field images are obtained according to the dark-field images. The classification of flaws and their sizes measurement based on bright-field images are also presented. Experiments show that the instrument can scan an optical element with the size of 810mm×460mm in less than 6 minutes and the inspection precision can reach 3μm.

***Index Terms*—Flaw inspection, Dark-field imaging system, Bright-field imaging system, Path planning, Image processing, Measurement, Large aperture optical element.**

I Introduction

Precision optical elements are widely used in the field of high energy optical devices, low light level imaging systems and semiconductor manufacturing [1]. During the process of producing, clean and transportation, the surfaces of precision optical elements will appear various types of flaws, such as pits, scratches, fiber, water stains and others. Those surface flaws increase the loss of light energy, and also affect the performance of the optical system. Therefore, surface flaw inspection for precision optical elements draws much attention in the field of optical engineering.

The method of automated visual inspection (AVI) is commonly used in surface inspection for various fields such as textiles, paper, semiconductor wafers, rail heads and concrete materials [2-6]. Generally, the general inspection devices which are used for precision optical elements such as the atomic force microscope (AFM) and scanning tunnel microscope (STM) have high precision, but also have shortcomings such as small measure range, low efficiency, high cost of the instrument and maintenance. So they are not suitable for surface flaw inspection for large aperture optical elements.

Currently, devices based on AVI are very common for the precision optical elements. For example, final optics damage inspection system [7, 8] which was employed in the National Ignition Facility to inspect flaws for the final optics and the digitizing surface flaw inspection system for optical elements in [9] adopted the dark-field imaging system (DFIS). In [10], the inspecting device used the dark-field back illumination and a camera with the resolution of 21 million pixels to get flaws information for the full size of optics in one time. The advantage of DFIS is easy to observe and detect small surface flaws due to the scattering amplification effect. Nonetheless, it brings many problems such as size distortion and classification failure of flaws. The relationship between the scattering image size and the actual size of the flaw in dark-field is complicated [11]. The calibration of actual size of flaws in dark-field images is needed for surface flaw inspection in order to get the real information of flaws. Indeed, there are some methods to measure the dark-field size [12-14]. However, they are not suitable for real time size calibration because of low accuracy and efficiency. Compared to DFIS, the bright-field imaging system (BFIS) is also widely used especially in the detection of cell [15-16]. This method generally uses a microscopic camera, so it is particularly suitable for small area detection and doesn't apply to large areas due to the impact of high resolution.

Rapid detection speed and high detection accuracy are prerequisites of detection device for large aperture optical elements. When the size of the optical element is 810×460mm, the device in [9] takes one hour for image acquisition and the number of sub aperture images is more than 3,700 which could affect the accuracy of image stitching. For large aperture optical elements, efficient algorithms of image display and processing are essential to ensure real time flaws inspections. In general, the distinction of surface flaws is most concerned by the inspector. However, the existing equipments [14], [17] can just only give the classification between pits and scratches instead of significant flaws such as pits and dusts.

The motivation of this work is to design a surface flaw inspection instrument for large aperture optical elements which can quickly inspect and give accurate information in detail. It integrates two different resolution imaging units for both advantages. One is BFIS which is constructed by a microscopic lens, a coaxial light source and an area scanning charge-coupled device (CCD) camera with 0.85μm resolution. The other is DFIS which is constructed by a linear light source and a line scan camera with 10μm resolution. The DFIS is developed to scan the whole optical element to quickly get all the distribution of surface flaws for coarse detection. The BFIS is used to measure the size of flaws and recognize the type for fine detection. Thus, this method meets the requirements of

This work is partly supported by National Natural Science Foundation of China under Grant 61473293, 61227804, 61421004, and 61305115. All authors are with the Research Center of Precision Sensing and Control, Institute of Automation, Chinese Academy of Sciences, Beijing 100190 (Corresponding email: sdxude@yahoo.com, xiantaoia@gmail.com).

high accuracy and efficiency. In addition, this paper investigates some of the key issues, including the adaptive scanning path planning method for the line scan camera based on 4 points focusing method, the display and process of dark-field images, the BFIS path planning method according to dark-field images, the classification and size measurement of flaws based on bright-field images.

The rest of this paper is organized as follows. The two imaging systems and their structures are introduced in Section II. Then the configuration of the proposed system is given. Section III designs the method to acquire the dark-field images of the optical elements. In Section IV, the methods of displaying and detecting flaws for dark-field images are presented. Section V describes the BFIS path planning method according to dark-field images. The classification and size measurement of flaws based on bright-field images are also provided in Section V. Section VI gives the experiments and results. Finally, this paper is concluded in section VII.

II System Design

A DFIS and BFIS

The light source is placed at an angle to the optical element so that the most of the light is reflected to the camera in BFIS, as shown in Fig. 1(a). In DFIS, the light source is placed in a way that the most of the light is reflected away from the camera, and only light of certain parts of the optical elements is reflected to the camera, as shown in Fig. 1(b). In this paper, the directed front light illumination is used for DFIS and a coaxial telecentric illumination is used for BFIS. In the dark-field system, even flaw size below the diffraction limit of the optical system, the flaw can still be detected when the intensity of scattered light is strong enough. Therefore, DFIS is more suitable for inspecting optical surface flaws. But scattering effects in DFIS make flaw size be not accurate. Fortunately BFIS can well solve this problem. Therefore, only one imaging system is hard to get reliable inspecting effects, so this paper presents a scheme combined DFIS and BFIS.

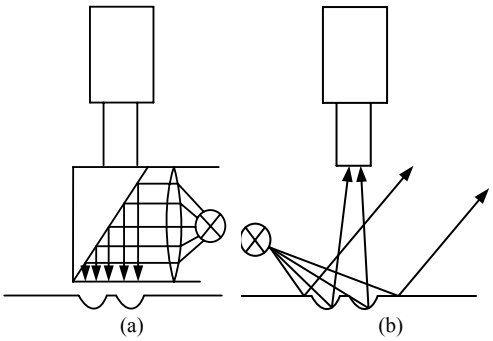

Fig. 1 Imaging system, (a) BFIS, and (b) DFIS

B System Design Combination with DFIS and BFIS

The proposed surface flaw inspection instrument for large aperture optical elements is composed of a clamp adjusting unit, a three dimensional motion unit, two visual units, and a host computer. The instrument setup is shown in Fig. 2.

The clamp adjustment unit can adapt to different sizes and types of optical elements, which is used to manually adjust yaw (θ_x) and pitch (θ_y) to ensure that the plane of optical element is perpendicular to the optical axes of cameras in visual units. The three-dimensional (3-D) movement unit consists of a three degree- of-freedoms (DOFs) motion platform. The horizontal axis represents the movement direction of X and the vertical axis represents the movement direction of Y. The focusing direction of the line scan camera and microscopic camera represents the movement direction of Z. The visual units consist of DFIS and BFIS. The collimated light source beside the visual units is the basis for the clamp to adjust the pose of the optical element according to the light transmission and reflection coincidence. The visual units are placed on vertical movement axis. The optical axes of the line scan camera, the microscopic camera and the collimating light component are parallel to each other. The computer is used to control the three DOFs motion platform and capture images.

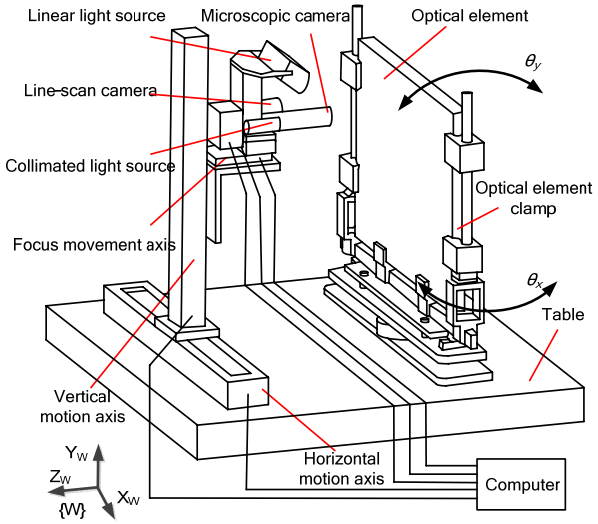

Fig. 2 Instrument configuration sketch

C Inspection Procedure

The task of this work is to inspect surface flaws for large aperture optical elements. The flow chart of the inspecting process can be divided into four stages, as shown in Fig. 3.

In stage-1, the optical element's pose must be manually adjusted by using the clamp adjusting unit and the collimated light source. After the pose adjusting of the optical element, it can be considered that its surface plane is basically perpendicular to the optical axes of cameras. Then, the motion path of the visual units is planned in stage-2. In this stage, the compensation amounts in the focus direction are calculated using the method described in section III. In stage-3, the motion platform is moved to capture dark-field images with the compensation amounts in the focus direction and the image in block is saved meanwhile. Thence, the full dark-field image can be formed by stitching all of the block images. In stage-4, preliminary flaws results of position information are obtained by processing dark-field images using the method described in section IV. In order to obtain further information such as the actual sizes and types of the flaws, the BFIS path planning method based on the dark-field image is used to capture the corresponding bright-field (BF) image. Based on the high resolution BF images, the sizes of flaws are obtained and their

classification is completed utilizing kernel ridge regression (KRR) based on geometric features and texture features. The areas of the flaw images in DFIS are replaced with the color reversed images in BFIS to form a whole surface image of the optical element with all flaws. Finally, the inspection information of all flaws on the large aperture optical element is obtained. In addition, the region of interest (ROI) of the entire image can be easily displayed in the interactive software by moving the mouse once the dark-field image acquisition is finished.

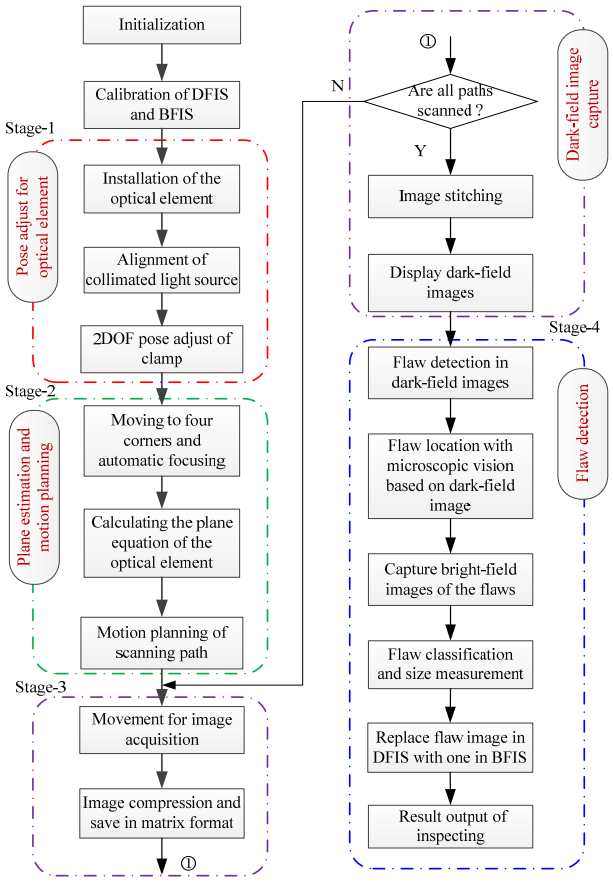

Fig. 3 Flow chart of the inspecting process

III Dark-Field Image Acquisition

A Adaptive Scanning Path Planning

A poly line moving scanning trajectory is designed to scan quickly. Firstly, the line scan camera starts from the left edge of the optical element, and then scanning along the Y axis to acquire images until the bottom edge. Secondly, the line scan camera moves the distance of the view field in the X direction, and then returns to the top edge along the Y axis. In this process, the scanned images are divided into blocks to be compressed and saved. Each block is with the size of 2048×2048 in pixel. One large column of image is formed with the blocks. The above procedure is repeated until the line scan camera is moved to the bottom right edge of the optical element, where the entire scanning process with DFIS is finished.

The large columns of images in accordance with the acquisition order can be named C_1, C_2, ... C_i ... C_n. The depth of view field of the line scan camera and the micro camera are 1mm and 40μm. Since the size of the optical element is too large, the angle error still remains after clamp adjusting. Moreover, the scanning plane isn't parallel to the surface plane of the optical element. So the line scan camera will be out of focus resulting in the unclear images. An adaptive scanning path planning method is proposed to correct the focus based on the above scanning trajectory in order to ensure that the images are always clear in the scanning process.

Firstly, it's necessary to select the four corner points of the optical element (top left corner, bottom left corner, top right corner, bottom right corner) to focus the microscopic camera in BFIS respectively. The function based on the *Sobel* operator is employed to judge the image sharpness in the focusing process. The microscopic camera is focused when the image sharpness function reaches maximum [18]. The positions of the motion system are recorded when the microscopic camera is separately focused at the four corner points.

With the four positions corresponding to the four corners, the surface plane equation of the optical element in the motion coordinate system can be obtained as given in (1). Therefore, the amount of focus adjustment in each scanning column can be calculated in (2) in order to ensure the line scan camera is focused.

$$ax + by + cz + 1 = 0 \tag{1}$$

where *a, b, c* are the plane parameters of the optical element.

$$\Delta z = -\frac{a\Delta x + b\Delta y}{c} \tag{2}$$

where Δz is the focusing adjustment, and Δx is the amount of motion in the X direction with respect to the scanning starting point, Δy is the amount of motion in the Y direction with respect to the scanning starting point.

B Motion Control of Dark-Field Image Acquisition

The amount of focusing adjustment is calculated in (2) when the line scan camera moves to scan the optical element. Then, the amounts of 3-D movement are sent into the motion platform for image acquisition. The grating ruler in Y axis is used as an external signal to trigger the line scan camera to capture dark-field images. Trigger frequency f is determined by the pixel equivalent which is specified in meters per scan line.

The accuracy of image acquisition in Y direction is guaranteed by using the grating ruler trigger signal driving the line scan camera. Accuracy of image acquisition in X direction is ensured by redundancy acquisition. The size of redundancy between two adjacent columns is d. In this work, the actual stitching offset $\Delta s_x[i]$ and $\Delta s_y[i]$ are calculated via feature matching between two adjacent columns i and i+1 using SIFT algorithm [19]. The whole dark-field image can be obtained by stitching these sub images together based on the offsets.

IV Display And Flaw Detection Of Dark-Field Image

There are a lot of sub images after image capturing. The size of a single sub image is 2048×2048 in pixel and covers 19.5×19.5mm, the gray level is represented with 8 bit, so the sub image needs 4M byte memory. If the optical element is

800×400mm, the entire image occupies about 3.2G byte memories. In the actual detection, the same element may need inspecting for different times. So a large amount of data generated in this way will have trouble in image storage and display. Those images should be compressed depending on the JPEG format before saved. And it is also no need to load all the images into memory disposable for displaying and processing. To solve this problem, a method for displaying and processing dark-field image is proposed as follows.

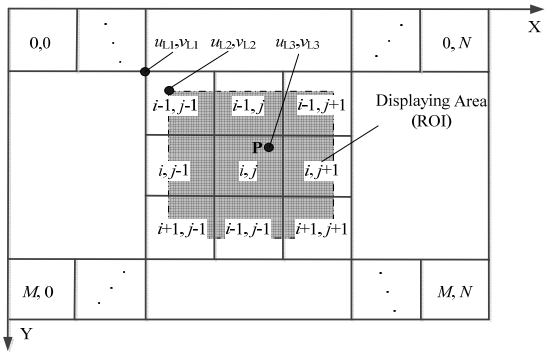

Fig. 4 The display principle of dark-field images

As showed in Fig. 4, the entire image is divided into (M +1) × (N +1) block sub images as the matrix format. Moreover, those sub images are all obtained after image stitching. In order to display and analysis of flaws conveniently, nine sub images (3×3 areas) are selected to load into memory for display. In order to display the region of interest, the serial number of nine sub images should be calculated before loading images into the memory. The serial number (i, j) is the center of nine sub images which contains the point P in Fig. 4. Assuming the point P is the center of a flaw. When the display area is changed, the number of nine sub images will be changed based on the center of the flaw. But the number of loading images is still 9 and the memory consumption doesn't increase. Then, the pixel coordinates (u_L, v_L) of the point P in the whole dark-field image after image stitching can be calculated in (3).

$$\begin{cases} u_L = u_{L1} + u_{L2} + u_{L3} \\ v_L = v_{L1} + v_{L2} + v_{L3} \end{cases} \tag{3}$$

where (u_{L1}, v_{L1}) is the image coordinates of the top left corner of 9 images relative to the whole dark filed image, and (u_{L2}, v_{L2}) is the image coordinates of the top left corner of ROI relative to the top left corner of 9 sub images. (u_{L3}, v_{L3}) is the image coordinates of point P in the ROI.

The process of flaws detection is proposed as follows. Firstly, all the dark-field images are binarized with a fixed threshold I_T. The areas with high gray values larger than I_T belong to the flaws. The flaws' edges in the area of 3×3 sub images are detected using the freeman chain code [20, 21] with the order of the matrix format. To avoid a flaw dividing into two or more parts in the 3 ×3 sub images area, it is needed to match and integrate the flaw contour. According to whether the points of flaw contour are in the 3×3 sub images area boundary or not, the contours of flaws are divided into F_1 and F_2. F_1 means the complete contours. F_2 does not. The mutual distance between the two contours is used in determining whether they are the same flaw or not. The Euclidean distance of two points on each contour is defined as the mutual distance. The integration principle of flaws is defined by

$$I_f = \begin{cases} 1, & if \quad D(A,B) \le D_T \\ 0, & if \quad D(A,B) > D_T \end{cases} \tag{4}$$

where I_f is the flag for contour integration, and $D(A, B)$ is the mutual distance between the two contours A and B, D_T is the threshold of contour integration.

V FINE INSPECTION OF FLAWS BASED ON BFIS

A BFIS Path Planning According to Dark-Field Images

The world coordinate system {W} and the motion coordinate system {M} are established on the motion platform. The origin of the motion coordinate system is the original point of machinery of the movement axis. The camera coordinates {L} and {C} are established on imaging planes of corresponding cameras with origins being the intersection of optical axes and imaging planes. The X_L axis and Y_L axis are corresponding to the u and v axes on the dark-field image. The X_C axis and Y_C axis are corresponding to the u and v axes on the bright-field image.

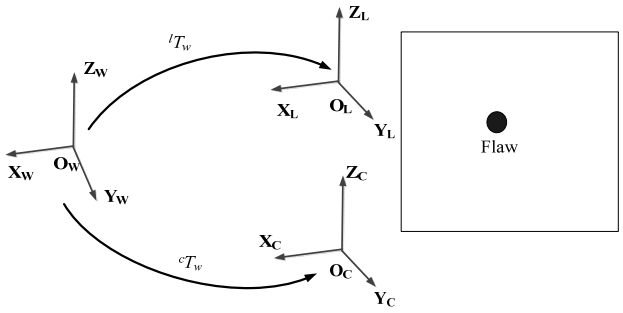

Fig. 5 Relation of flaw point and camera frame

In Fig. 5, ^lT_w is the extrinsic parameter matrix of the line scan camera and ^cT_w is the extrinsic parameter matrix of the microscopic camera. After the dark-field image acquisition, our goal is that the microscopic camera can automatically move to corresponding flaw position for detail observing by choosing the flaws in the dark-field image. To achieve this purpose, the relationship between the coordinates of the world and the image coordinates in two cameras should be obtained.

To obtain the model for the interior geometry of the line scan camera, we can regard a line sensor as one particular line of an area sensor. Therefore, like a traditional camera, suppose that the line scan camera is with negligible lens distortion. Its intrinsic property can be described with the pinhole model. In process of a scanning column, the four parameter model of the line scan camera can be given as

$$\begin{bmatrix} u_{li} \\ v_{li} \\ 1 \end{bmatrix} = \begin{bmatrix} k_{lx} & 0 & u_{l0} \\ 0 & k_{ly} & v_{l0} \\ 0 & 0 & 1 \end{bmatrix} \begin{bmatrix} x_l / z_l \\ y_l / z_l \\ 1 \end{bmatrix} \tag{5}$$

where (u_{li}, v_{li}) are the coordinates of a point in the scanning column i of the dark-field image, (u_{l0}, v_{l0}) denote the image coordinates of the line scan camera's principal point, (x_l, y_l, z_l) are the coordinates of the point in the line scan camera frame, and k_{lx} and k_{ly} are the magnification coefficients from the imaging plane coordinates to the image coordinate.

The transformation from the line scan camera frame to the world frame is known as the extrinsic parameters for the line scan camera.

$$\begin{bmatrix} x_l \\ y_l \\ z_l \\ 1 \end{bmatrix} = \begin{bmatrix} {}^{l}n_{wx} & {}^{l}o_{wx} & {}^{l}a_{wx} & {}^{l}p_{wx} \\ {}^{l}n_{wy} & {}^{l}o_{wy} & {}^{l}a_{wy} & {}^{l}p_{wy} \\ {}^{l}n_{wz} & {}^{l}o_{wz} & {}^{l}a_{wz} & {}^{l}p_{wz} \\ 0 & 0 & 0 & 1 \end{bmatrix} \begin{bmatrix} x_w \\ y_w \\ z_w \\ 1 \end{bmatrix} = {}^{l}T_w \begin{bmatrix} x_w \\ y_w \\ z_w \\ 1 \end{bmatrix} \tag{6}$$

where (x_w, y_w, z_w) are the coordinates of the point in the world frame, ${}^{l}T_w$ is the extrinsic parameter matrix of the line scan camera.

Similarly, the microscopic camera also has the intrinsic parameter matrix and extrinsic parameter matrix. Since the two optical axes of cameras are parallel to each other, the rotation angle between the two coordinate systems is negligible. Therefore, the relationship between the two camera coordinate systems can be expressed as:

$${}^{c}T_l = \begin{bmatrix} 1 & 0 & 0 & {}^{c}p_{lx} \\ 0 & 1 & 0 & {}^{c}p_{ly} \\ 0 & 0 & 1 & {}^{c}p_{lz} \\ 0 & 0 & 0 & 1 \end{bmatrix} \tag{7}$$

where ${}^{c}p_l = [{}^{c}p_{lx}\ {}^{c}p_{ly}\ {}^{c}p_{lz}]^{\mathrm{T}}$ is the position vector of the origin O_l, expressed in the microscopic camera frame.

The rotation angle in (6) between the line scan camera coordinate system and the world coordinate system is also negligible for further simplification. It can be thought that the two cameras are perpendicular to the plane of the optical element. Based on the above conditions, the re-positioning model can be simplified to:

$$\begin{aligned} x_w &= \frac{(u_{li} - u_{l0}){}^{l}p_{wz}}{k_{lx}} + {}^{c}p_{lx} = \delta_{lx}(u_{li} - u_{l0}) + {}^{c}p_{lx} \\ y_w &= \frac{(v_{li} - v_{l0}){}^{l}p_{wz}}{k_{ly}} + {}^{c}p_{ly} = \delta_{ly}(v_{li} - v_{l0}) + {}^{c}p_{ly} \end{aligned} \tag{8}$$

where (x_w, y_w) is the coordinates of the flaw in {W}, (u_{li}, v_{li}) is its pixel coordinates in the scanning column i of the dark-field image, δ_{lx} and δ_{ly} are the pixel equivalents of the line scan camera.

The motion platform can be controlled to move the microscopic camera to observe the flaw based on (8). The relationship of the image coordinates u_{li} and the corresponding flaw points in world coordinates x_w can be obtained by the formulas (5) and (6) and z_w=0.

$$u_{li} = k_{lx}\frac{x_w + {}^{l}p_{wx}}{{}^{l}p_{wz}} + u_{l0} \tag{9}$$

Due to the continuous focusing movement in a large column of image acquisition procedure, the amount of focus adjustment in (2) has error. Formula (9) is rewritten as

$$u_{li} = k_{lx}\frac{x_w' + {}^{l}p_{wx}}{{}^{l}p_{wz} + \Delta{}^{l}p_{wz}} + u_{l0} \tag{10}$$

where $\Delta{}^{l}p_w$ is the variable quantity of ${}^{l}p_w$ caused by the errors of focusing motion.

The relationship between the point u_{li} in the scanning column i of the dark-field image and the re-positioning error in horizontal direction caused by focusing motion can be expressed as

$$\Delta x_{wz} = x_{wz}' - x_{wz} = \frac{\Delta{}^{l}p_{wz}(u_{li} - u_{l0})}{k_{lx}} \tag{11}$$

where Δx_{wz} is the re-positioning error caused by focusing motion in the horizontal direction.

The whole dark-field image is obtained by stitching adjacent scanning columns together. The stitching error also affects the re-positioning error which can be expressed as

$$\Delta x_{wu} = \frac{{}^{l}p_{wz}\sum_{k=1}^{i-1} e_u(k)}{k_{lx}} \tag{12}$$

where Δx_{wu} is the re-positioning error caused by stitching error in the horizontal direction. $e_u[k]$ is the stitching error in the scanning column k.

The relationship between the pixels coordinate and positioning error can be expressed as

$$\Delta x_w = \Delta x_{wz} + \Delta x_{wu} = \frac{\Delta{}^{l}p_{wz}(u_{li} - u_{l0})}{k_{lx}} + \frac{{}^{l}p_{wz}\sum_{k=1}^{i-1} e_u(k)}{k_{lx}} \tag{13}$$

where Δx_w is the total re-positioning error.

Generally, $\Delta{}^{l}p_w$ isn't constant because of installation errors in the instrument and return errors during motion. The angle still exists between the camera imaging plane and the plane of the optical element after the clamp adjustment. The stitching errors in each scanning column are not the linear relationship in practical applications, so the relationship between the pixels coordinate and positioning error is close to a non-linear relationship which can be fitted by polynomial fitting.

$$\Delta x_w = a_n u_{li}^{\ n} + a_{n-1}u_{li}^{\ n-1} + \ldots\ldots a_1 u_{li} + a_0 \tag{14}$$

where a_0, a_1,…, a_n are the parameters of the non-linear relationship.

B Flaw Size Measurement Based on Bright-Field Image

Since the microscope in BFIS can be calibrated by optical measurement microscope in advance, the actual size of flaws can be achieved using the bright-field image. The above method is used to guide the microscopic camera to automatically capture corresponding bright-field image. So the actual size of the *j*-th flaw can be obtained as given in (15).

$$\begin{cases} l_j = \delta_{cx} \times N_L \\ w_j = \delta_{cy} \times N_W \end{cases} \tag{15}$$

where δ_{cx} and δ_{cy} are pixel equivalents of microscopic camera, the pixel size of *j*-th flaw in the bright-field image is $N_L \times N_W$, the actual size of the *j*-th flaw is $l_j \times w_j$, the unit is μm.

The bright-field image of the flaw is necessary to be preserved, so that the optical element can be analyzed and processed off line in any time with no optical element in the inspecting instrument. However, sometimes the optical element has a lot of flaws and the bright-field images commonly have high resolution, it is unnecessary to save all the bright-field images directly for analyzing because of low efficiency and waste memory. The method replacing the flaw image in DFIS with one in BFIS is used. In this way, a whole surface image of the optical element with all flaws is obtained in bright-field and dark-field images fusion method. The pixel size of the flaw in dark-field image can also be calculated in (16) as the condition of off line.

$$\begin{cases} N_L' = \dfrac{\delta_{cx} \times N_L}{\delta_{lx}} \\ N_W' = \dfrac{\delta_{cy} \times N_W}{\delta_{ly}} \end{cases} \tag{16}$$

where δ_{lx} and δ_{ly} are pixel equivalents of the line scan camera, the pixel size of *j*-th flaw in the dark-field image is $N_L' \times N_W'$.

C Classification between Dust and Pit

In general, the main defects in the optical elements can be divided into three categories: pits, scratches and dusts. The distinction of dusts and pits in most of surface flaws are most concerned by the inspector. Because both forms are similar, it is easy to misjudge each other which could affect the reliability of the inspecting system. The scattering effect of dust is similar to pits. The imaging results in the dark-field image as shown in Fig. 6(a) and 6(b). It is difficult to distinguish in this condition. However, the dusts in the bright-field image have the smooth texture and a uniform luminance distribution, but the texture of pits in the bright-field image is much vague and has uneven brightness distribution as shown in Fig. 6(c) and 6(d).

The shapes of scratches are different from pits and dusts, the textures of dusts and pits are different. Two kinds of features, i.e. geometric features and texture features, are selected to recognize flaws. The geometric features of flaws are selected according to experience as follows: the length of the flaw's contour l, the aspect ratio of the flaw's minimum bounding rectangle r_1, the ratio of the flaw's area and the area of the flaw's minimum bounding rectangle r_2, the perimeter of the flaw's contour c. Those features are selected in bright-field image instead of dark-field image. It is not all damages that can be identified by only geometric features. So texture features are necessary. Five dimensional texture features are selected in the bright-field image as follows.

1) Gray value:

$$M = \frac{1}{n} \sum_x \sum_y f(x, y) \tag{17}$$

2) Gray scale standard deviation:

$$\sigma = \sqrt{\frac{1}{n} \sum_x \sum_y [f(x, y) - M]^2} \tag{18}$$

3) Contrast:

$$C = \sum_i \sum_j (i - j)^2 P(i, j) \tag{19}$$

4) Energy:

$$A = \sum_i \sum_j (i - j)^2 P(i, j) \tag{20}$$

5) Entropy:

$$E = -\sum_i \sum_j P(i, j) \log P(i, j) \tag{21}$$

where $f(x, y)$ is the gray value of the pixel (x, y), P is the grey level co-occurrence matrix (GLCM) [22, 23] and $P(i, j)$ means the repeated intensity of gray value (i, j) in the image.

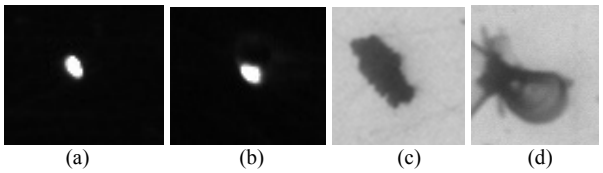

(a) (b) (c) (d)

Fig. 6 Typical flaws, (a) dust, (b) pit in dark-field image, (c) dust, (d) pit in bright-field image

Four geometric features such as the contour length l, the aspect ratio r_1, the area ratio r_2 and the perimeter c and five texture features such as M, σ, C, A and E in (17) to (21) are calculated. When the nine dimensional features are achieved, they are put into the classifier to classify the flaws using the kernel ridge regression (KRR) classifier [24-26].

In addition, the support vector machine (SVM) classifier [27, 28] is also effective for the classification of pits, scratches and dusts.

VI Experiments

A Experiment System

An experiment system (as shown in Fig. 7) was established according to the scheme given in section II. In the experiment system, two vision units were a Dalsa line scan camera and a PointGrey microscopic camera which equipped with a Navitar zoom lens with magnification 0.47~ 4.5×. The resolution of line scan camera was 8192 pixel and the maximum of line frequency was 68.6 KHz. The microscopic camera captured images 15 frames per second with image size of 1280×960 in pixel. The two cameras were placed on the motion platform and the focusing direction is along their optical axes. The

collimated light source was placed in parallel with the cameras. The clamp was mainly composed of a bolt and a bearing turntable for adjusting pose. The maximum size of the optical element for inspecting was 810×460mm. The CPU of the host computer was Intel Core^{TM}2 DUO with frequency of 2.8GHz.

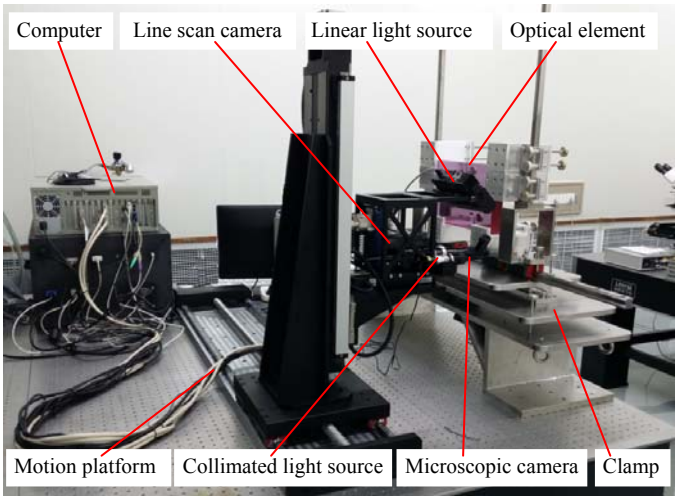

Fig. 7 Experiment system

B Image Acquisition and Flaws Detection

According to the scanning path presented in section III, the amount of focus adjustment in each scanning column needs to be generated at first. Before the image acquisition, four corner points were obtained to determine the parameters in (1) with least square method (LSM). The estimated plane parameters of the optical element were a = 0.0982, b= 0.0488, c= 16.3161. Redundancy d in the image acquisition was set to 3mm. In the dark-field image acquisition experiments, the processes were described in the flow chart in section II. The whole image of the optical element was successfully obtained in 6 minutes. The saved matrix was 24 × 42 and the whole number of scanning column was 11. It's sure that the inspecting instrument of the large aperture optical element has the great inspecting efficiency.

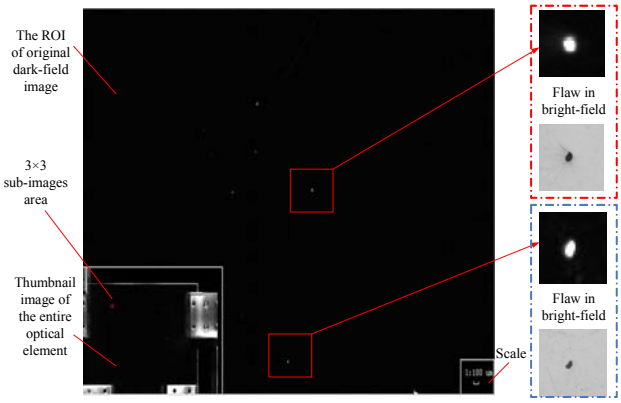

Fig. 8 The displaying result of dark-field image

The result of the dark-field image displaying in software is shown in Fig. 8. In the left bottom corner of the interface was the thumbnails of the entire dark-field image and the 3×3 sub images area was the small red rectangular in the thumbnails. The thumbnail gave a rough distribution of the surface damage of the optical element. The main displaying area was the ROI based on the 3×3 sub images area for fine inspection. The flaws in the dark-field image were the bright spots compared to the black background. On the right side of the dark-field image were the flaws imaged using the microscope.

In the experiment of flaws detection, the threshold I_T for the binarization was set to 30. The D_T was set to 2. Three dark-field images in Fig. 9 (a), 9(b) and 9(c) were the left part, right part and the full flaw. The image in Fig. 9(c) was the result of integration which was marked in green window. In this experiment, there was one wrong integration result caused by the border of the optical element. In fact, if an optical element had the border, it needed to remove the image of border during the integration process. All of the flaws can be properly integrated in this condition. It is sure that the robustness of flaws detection can meet the requirements of a practical system.

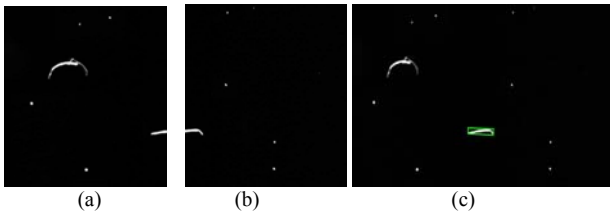

Fig. 9 Dark-field images, (a) ROI of numbered (2, 2), (b) ROI of numbered (2, 3), (3) ROI of dark-field image after integration

C Dark-Field Positioning Bright-Field Experiments

According to the location method presented in section V, the cameras' parameters needs to be calibrated at first. The pixel equivalents of the line scan camera were obtained by calibration board as follows: δ_{lx} = 9.48 μm/pixel, δ_{ly} =9.56 μm/pixel. The initial pose of the line scan camera with respect to the microscopic camera frame was measured. The result was as given in (22). The unit of the position vector in (22) is mm.

$$ {}^{c}T_{l} = \begin{bmatrix} 1 & 0 & 0 & 80.0 \\ 0 & 1 & 0 & 12.12 \\ 0 & 0 & 1 & 120.7 \\ 0 & 0 & 0 & 1 \end{bmatrix} \tag{22} $$

In experiments, 20 groups of u_{li} and Δx_w were obtained to determine the parameters in (14) with LSM. The 20 sets of data were selected in the same large column of the dark-field images. The estimated parameters in (14) were a_2= 9.2524 × 10^{-6}, a_1= -0.0268, a_0 = -64.89. The relationships between image pixel in a large column of the dark-field images and the positional error in the horizontal direction were shown in Fig. 10. Experimental results showed that the non-linear relationship was well fitted by a quadratic curve. The relationships between the image pixel and the positional errors in the vertical direction were also experimented with 20 groups of data. The result was shown in Fig. 11. It can be seen that positioning accuracy in the Y direction was higher than the positioning accuracy of the X

direction. As the Y direction was the direction of the line camera's movement which was triggered by the grating ruler, Y direction positioning was more accurate.

In fact, the estimated parameters in (14) at each large column of the dark-field images were not the same because of motion error. The same parameters were applied in the experiments for simplification. In experiments, 12 points were chosen randomly in whole dark filed image to observe the bright-field images of the flaws to verify the accuracy after the positioning compensation in the same parameters. The positioning accuracy of 12 points is shown in Fig. 12 and the actual and computed positions in the motion coordinates are shown in Fig. 13.

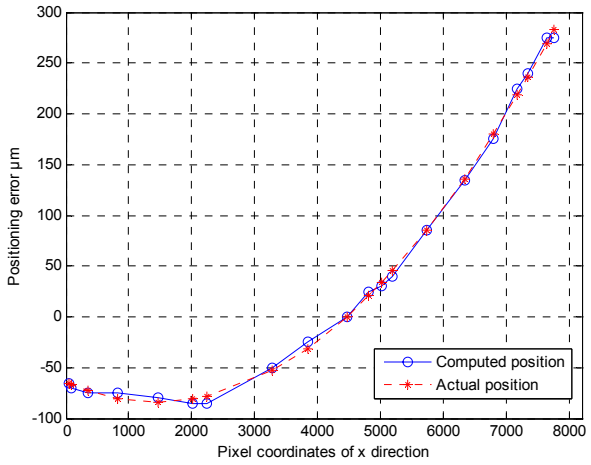

Fig. 10 The relationship between image pixels in a large column and the X positioning error

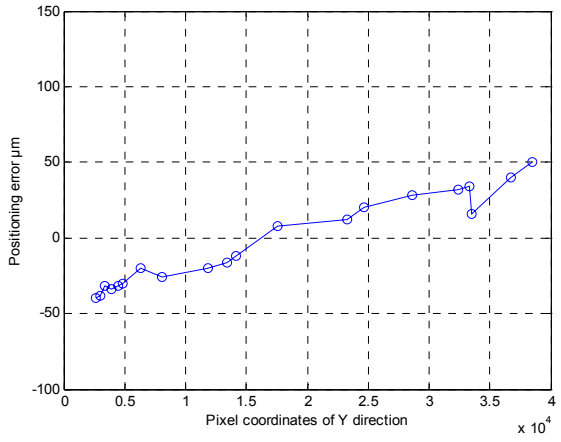

Fig. 11 The relationship between image pixels and the Y positioning error

The points marked with "*" were the computed positions of the flaws after positioning compensation with (14). The points marked with "o" were the actual positions of the flaws in the world coordinate system. The maximum positioning error along the X direction was 0.15mm. Therefore, the microscopic camera can be guided accurately to locate the flaws in the bright-field image with the amount of compensation in (14) for each scanning column. Since the view field of microscopic camera was 1×0.82mm, the position compensation value met the requirement that the flaws in BFIS were always in the central view field of the microscopic camera.

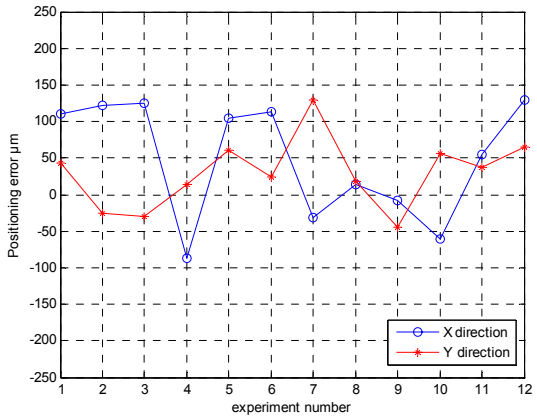

Fig. 12 Positioning errors in experiments

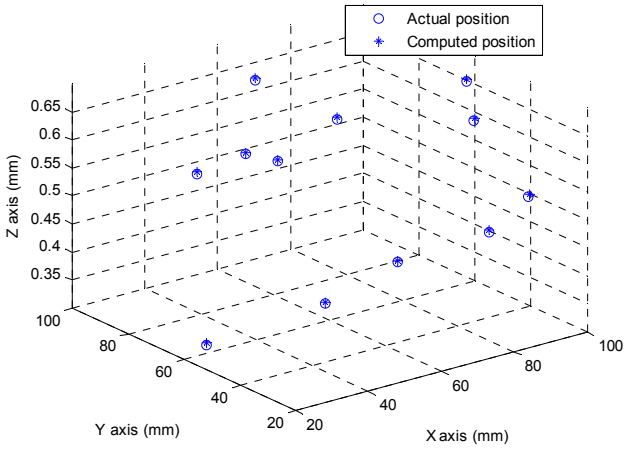

Fig. 13 Actual and computed position

D Flaws Size Measurement Experiment

In this experiment, 16 typical flaws were selected to conduct size measurement in the dark-field image using the method described in section VI. The bright-field images of flaws were obtained by the above method. Three kind images of three flaws were shown in Fig. 14. Fig. 14(a), 14(d) and 14(g) were the bright-field images of the flaws, 14(b), 14(e) and 14(h) were the dark-field images of the flaws, 14(c), 14(f) and 14(i) were the dark-field images after replaced. It can be seen that the shapes of the flaws in the original dark-field image had a large difference from ones in the bright-field image because of the scattering effect.

Table I listed the measured sizes in DFIS, in BFIS and actual sizes measured by the general measuring microscope off-line. The measured sizes in DFIS were calculated using Yang's method [14]. In [14], the relationship of the number of pixels in the dark-field image and the actual size of flaw is not a simple linear scaling relationship, but a complex multiple-item relationship. The standard contrast patterns were taken as the optical element which was used to calibrate the size. The patterns were circular shape. Their specifications were: diameter 50mm, thickness 8mm and the surface roughness 2.0nm. They were produced with the material as same as the optical element. Each pattern was divided into the 5×5mm blocks. The scratches and pits in different regions were made

with photolithography and etching techniques. The depth of each flaw was 250nm and the length was ranged from 10μm to 120μm. According to the experimental data, the scaling ratio between the standard sizes and the image pixels was obtained by polynomial curve fitting. The conversion function of Yang's method was $y= -0.143x^3-2.296x^2 +17.856x +13.302$. x was the pixel length in dark-field image, and y was the actual length of the flaw. The function y was suitable for a range from 20μm to 120μm.

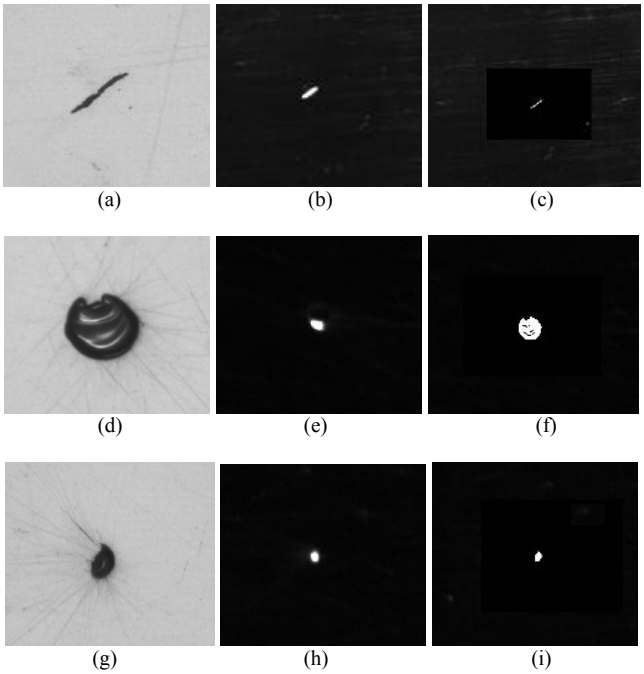

Fig. 14 Flaws, (a), (d), (g) in the bright-field image, (b), (e), (h) in the dark-field image, (c), (f), (i) in the dark-field image after replacement

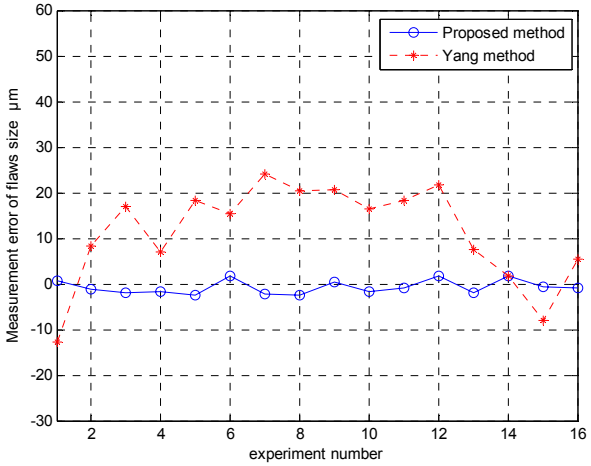

Fig. 15 Errors with the proposed method and Yang's method

The measured size in BFIS was obtained by (15). The parameters in (15) were obtained by calibration board as follows: $\delta_{cx} = \delta_{cy}$ =0.85μm/pixel. 16 flaws were chosen to measure their sizes in this experiment. From the Table I, we can find that some flaws had the same size measured in DFIS. But in fact they had a big difference in the sizes measured with BFIS. Due to scattering effect in dark-field, the flaws' sizes measured with DFIS were bigger than ones measured with BFIS. The results show that the errors in the measured sizes with BFIS were less than ones with Yang's method. A group of measuring results is shown in Fig. 15, in which the maximum error by Yang's method was about 25μm. The maximum error in proposed method was about 3μm.

E Flaws Classification Experiment

240 samples were selected as training samples, which included 100 dusts, 100 pits and 40 scratches. 200 samples were selected as the test samples which consisted of 80 dusts, 80 pits and 40 scratches. As the texture features were calculated by GLCM, the average statistic value in four directions 0°, 45°, 90° and 135° was selected as the value of texture feature in our method.

A comparative experiment was conducted. The comparative method was in [29], there were three features to classify flaws which contain elongation level, rectangular level and circularity level. Those features were all extracted from the dark-field images. The classifier was also the kernel ridge regression. The kernel function is a Gaussian function. The results were listed in Table II. It can be found that the recognition accuracy of our method was significantly higher than the method in [29], especially in the dust recognition. Because it was difficult to distinguish between dust and pit in the dark-field image as the similar features. In other words, the proposed classification in the bright-field image is more appropriate to identify surface flaws instead of the dark-field image.

TABLE I
MEASURED SIZES OF FLAWS

Index	DFIS[14] (μm)		BFIS (μm)		Actual (μm)
	Size	Error	Size	Error	
1	76.4	15.9	61.1	0.6	60.5
2	76.4	8.3	66.8	-1.3	68.1
3	57.3	17.0	38.2	-2.1	40.3
4	72.7	7.1	64.0	-1.6	65.6
5	34.4	18.3	13.5	-2.6	16.1
6	67.5	15.3	54.0	1.8	52.2
7	47.7	24.2	21.3	-2.2	23.5
8	51.4	20.4	28.6	-2.4	31.0
9	39.3	20.6	19.1	0.4	18.7
10	65.9	16.4	47.7	-1.8	49.5
11	57.3	18.3	38.2	-0.8	39.0
12	59.5	21.8	39.3	1.6	37.7
13	76.4	7.6	66.8	-2.0	68.8
14	57.3	1.7	57.3	1.7	55.6
15	105.2	9.1	95.5	-0.6	96.1
16	54.0	5.3	47.7	-1.0	48.7

TABLE II
RECOGNITION RESULT OF FLAWS

Method	Number of true positive			Number of false positive			Accuracy
	Pits	Dusts	Scratches	Pits	Dusts	Scratches	
Our method	76	74	39	4	6	1	94.5%
Method in [29]	72	48	38	8	32	2	79%

VII CONCLUSION

Our main contribution is that a novel surface flaw inspection instrument is designed based on two imaging systems which are BFIS and DFIS. The DFIS which is constructed by a line scan

camera is used in rapid detection and coarse inspection. The BFIS which is constructed by a microscopic camera is used in accurate detection and fine inspection. This instrument is designed for the optical elements with the sizes less than 810×460mm. It gets surface flaws information of an optical element in a fast and accurate way. An adaptive scanning path planning method for the line scan camera based on 4 points focusing method is proposed to keep the image clarity in the scan process with DFIS. A set of novel algorithms is proposed to display and analyze the dark-field images. The flaws positioning in the bright-field image guided with the dark-field image is achieved. The whole dark-field image with accurate flaw size is well obtained via replacing the images of the flaws in DFIS with ones in BFIS. The type classification of flaws is accurately identified in BFIS. Experimental results show that this instrument can meet the needs of efficiency and accuracy of inspection for large aperture optical elements.

REFERENCES

[1] T. A. Germer, C. Wolters, D. Brayton, "Calibration of wafer surface inspection systems using spherical silica nanoparticles," *Optics express,* vol. 16, no. 7, pp. 4698-4705, 2008.

[2] G. Santanu, M. Anirban, M. Gangadaran, "Automatic defect detection on hot rolled flat steel products," *IEEE Transactions on Instrumentation and Measurement*, vol. 62, no. 3, pp. 612-621, 2013.

[3] Q. Li, S. Ren, "A real time visual inspection system for discrete surface defects of rail heads," *IEEE Transactions on Instrumentation and Measurement*, vol. 61, no. 8, pp. 2189-2199, 2012.

[4] A. Yazaki, C. Kim, J. Chan, "Ultrafast dark field surface inspection with hybrid dispersion laser scanning," *Applied Physics Letters*, vol. 104, no .25, pp. 2511061-2511065, 2014.

[5] Z. Liu, M. Genest, D. S. Forsyth, A. Marincak, "Quantifying surface deformation with the edge of light enhanced visual inspection," *IEEE Transactions on Instrumentation and Measurement*, vol. 58, no. 2, pp. 416-422, 2009.

[6] C. C. Wang, B. C. Jiang, J. Y. Lin, C. C. Chu, "Machine vision based defect detection in IC images using the partial information correlation coefficient," *IEEE Transactions on Semiconductor Manufacturing*, vol. 26, no. 3, pp. 378-384, 2013.

[7] A. Conder, J. Chang, L. Kegelmeyer, M. Spaeth, P. Whitman, "Final optics damage inspection (FODI) for the national ignition facility," *International Society for Optics and Photonics*, vol. IV, pp. 77970-77982, 2010.

[8] C. J. Stolz, "Status of NIF mirror technologies for completion of the NIF facility," *Advances in Optical Thin Films IIIi*. Vol. 7101, pp. 7101151-71011511, 2008.

[9] F. Wang, Y. Yang, D. Sun, L. Yang, R. Li, "Digital realization of precision surface defect evaluation system," In *the Proceedings of 2006 International Symposium on Advanced Optical Manufacturing and Testing Technologies*, Xian, China, Nov. 1-5, 2006, pp. 61500F1-61500F5.

[10] Y. Fan, N. Chen, L. Gao, "Digital detection system of surface defects for large aperture optical elements," *High Power Laser and Particle beams*, vol. 21, no. 7, pp. 1032-1036, 2009.

[11] C. Yen, C. Hung, "Dark field inspection technique on poly silicon CMP process," In *the Proceedings of 2012 e Manufacturing & Design Collaboration Symposium,* Taiwan, Sep. 4, 2012, pp. 1-2.

[12] R. R. Prasad, M. Bernacil, J. Halpin, J. Peterson, S. Mills, R. P. Hackel, "Design of an illumination technique to improve the identification of surface flaws on optics," *Boulder Damage Symposium*, vol. VI, pp. 421-426, 2005.

[13] X. Cheng, X. Xu, and L. Zhang, "Defect testing of large aperture optics based on high resolution CCD camera." *High Power Laser and Particle beams*, vol. 21, no. 11, pp. 1677-1680, 2009.

[14] Y. Yang, C. Lu, and J. Liang, "Microscopic dark field scattering imaging and digitalization evaluation system of defects on optical devices precision surface," *Acta Optica Sinic*a, vol. 27, no. 6, pp. 1031-1038, 2007.

[15] F. Mualla, S. Scholl, B. Sommerfeldt, "Automatic cell detection in bright field microscope images using SIFT, random forests, and hierarchical clustering," *IEEE Transactions on Medical Imaging*, vol. 32, no. 12, pp. 2274-2286, 2013.

[16] C. Zhang, F. Huber, "Yeast cell detection and segmentation in bright field microscopy," In *the Proceedings of 2014 11th International Symposium on Biomedical Imaging*, Beijing, China, Apr. 29-May. 2, 2014, pp. 1267-1270.

[17] H. Chu, Z. Xie, Q. Liu, Y. Shao, "Surface cleanliness inspection apparatus for optical component based on machine vision," In *the Proceedings of 2010 3th International Congress on Image and Signal Processing*, Yantai, China , Oct. 16-18, 2010, pp. 1694-1698.

[18] L. Liu, Y. Zheng, J. Feng, "Fast auto focusing technique for multi objective situation," In *the Proceedings of 2010 International Symposium on Computer Application and System Modeling*, Taiyuan, China, Oct. 22-24, 2010, pp. 607-610.

[19] D. G. Lowe, "Distinctive image features from scale invariant keypoints," *International journal of computer vision*, vol. l60, no. 2, pp. 91-110, 2004.

[20] X. Lan, D. Shu, "Circle and circular arc detection algorithm research based on Freeman chain code", In *the Proceedings of 2013 Electronics Information and Emergency Communication*, Beijing, China, Nov. 15-17, 2013, pp. 230-233.

[21] J. Onishi, T. Ono, "Contour pattern recognition through auditory labels of freeman chain codes for people with visual impairments," In *the Proceedings of the 2011 International Conference on Systems, Man, and Cybernetics*, Alaska, USA, Oct. 9-12, 2011, pp. 1088-1093.

[22] G. Liu, R. Wang, Y. Deng, R. Chen, Y. Shao, Z. Yuan, "A new quality map for 2-D phase unwrapping based on gray level co-occurrence matrix," *Geoscience and Remote Sensing Letters*, vol. 11, no. 2, pp. 444-448, 2014.

[23] P. Kunakornvong, C. Tangkongkiet, P. Sooraksa, "Defect detection on air bearing surface with gray level co occurrence matrix," In *the Proceedings of 2014 Information and Communication Technology, Electronic and Electrical Engineering*, Chiang Rai, Thailand, Mar. 5-8, 2014, pp.1-4.

[24] J. Sen, W. Liu, and S. Venkates, "Face recognition using kernel ridge regression," In *the Proceedings of 2007 IEEE Conference on Computer Vision and Pattern Recognition*, Minneapolis, USA, Jun. 17-22, 2007, pp. 1-7.

[25] Y. Gu, C. Wang, B. Liu, Y. Zhang, "A kernel based nonparametric regression method for clutter removal in infrared small target detection applications," *Geoscience and Remote Sensing Letters*, vol. 7, no. 3, pp. 469-473, 2010.

[26] J. He, L. Ding, L. Jiang, L. Ma, Kernel ridge regression classification, *2014 International Joint Conference on Neural Networks*, Beijing, China, July 6-11, 2014, pp. 2263-2267.

[27] J. M. Chang, C.-C. Fang, K.-H. Ho, N. Kelly, *et al*, Capturing cognitive fingerprints from keystroke dynamics, *IT Professional*, vol. 15, no. 4, pp. 24-28, 2013.

[28] M. Maalouf, D. Homouz, Kernel ridge regression using truncated Newton method, *Knowledge-Based Systems*, vol. 71, pp. 339-344, 2014.

[29] C. Yang, R. Lu, N. Chen, "A fast method for large aperture optical elements surface defects detection." In *the Proceedings of the 2011 MESC International Conference on Multimedia*, *Software Engineering and Computing*, Wuhan, China, Nov. 26-27, 2011, pp. 175-184.

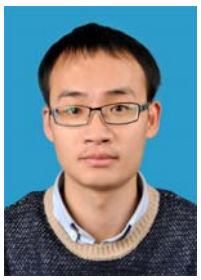

Xian Tao received the B. Sc. degree from Shaanxi University of Science and Technology, Xian, China, in 2010 and the M.Sc. degree from China University of Mining and Technology, Beijing, China, in 2013, both in mechanical and automotive engineering. He is currently working toward Ph. D degree at Institute of Automation, Chinese Academy of Sciences (IACAS), in control science and engineering. His current research interests include computer vision and automation.

Zhengtao Zhang received the B. Sc. degree from China University of Petroleum, Dongying, China, in 2004, and M. Sc. degree from Beijing Institute of Technology, Beijing, China, in 2007, and the Ph. D. degree from IACAS, Beijing, China, in 2010, all in control science and engineering. He is a Professor in the Research Center of Precision Sensing and Control, IACAS. His research interests include visual measurement, micro-assembly, and automation.

Feng Zhang received the B. Sc. degree from Qingdao University, Qingdao, China, in 2006, and the Ph. D. degree from IACAS, Beijing, China, in 2012, all in control science and engineering. He is an Assistant Professor in the Research Center of Precision Sensing and Control, IACAS. His research interests include robot control, biomedical signal processing and functional electrical stimulation.

De Xu (M'05-SM'09) received the B. Sc. and M. Sc. degrees from Shandong University of Technology, Jinan, China, in 1985 and 1990, respectively, and the Ph. D. degree from Zhejiang University, Hangzhou, China, in 2001, all in control science and engineering. He has been with IACAS since 2001.

He is currently a Professor in the Research Center of Precision Sensing and Control, IACAS. His current research interests include robotics and automation such as visual measurement, visual control, intelligent control, welding seam tracking, visual positioning, microscopic vision, micro-assembly.